Performance and Sensitivity of the BICEP Array 150 GHz Receiver

S. Zhang[a], BICEP/*Keck* Collaboration:
P. A. R. Ade[b], Z. Ahmed[c,d], M. Amiri[e], D. Barkats[f], R. Basu Thakur[a], C. A. Bischoff[g], D. Beck[h,*], J. J. Bock[a,i], H. Boenish[f], V. Buza[j], B. Cantrall[h,c], J. R. Cheshire IV[a], J. Connors[k], J. Cornelison[l], M. Crumrine[m], A. J. Cukierman[a], E. Denison[k], L. Duband[n], M. Echter[f], M. Eiben[f], B. D. Elwood[o,f], S. Fatigoni[a], J. P. Filippini[p,q], A. Fortes[h], M. Gao[a], C. Giannakopoulos[g], N. Goeckner-Wald[h], D. C. Goldfinger[h], S. Gratton[r,s], J. A. Grayson[h], A. Greathouse[a], P. K. Grimes[f], G. Hall[t,h], G. Halal[h], M. Halpern[e], E. Hand[g], S. A. Harrison[f], S. Henderson[c,d], T. D. Hoang[m], J. Hubmayr[k], H. Hui[a], K. D. Irwin[h], J. H. Kang[a], K. S. Karkare[u,c,d], S. Kefeli[a], J. M. Kovac[o,f], C. Kuo[h], K. Lasko[m,t], K. Lau[a], M. Lautzenhiser[g], A. Lennox[q], T. Liu[h], S. Mackey[j], N. Maher[m], K. G. Megerian[i], L. Minutolo[a], L. Moncelsi[a], Y. Nakato[h], H. T. Nguyen[i,a], R. O'Brient[i,a], S. N. Paine[f], A. Patel[a], M. A. Petroff[f], A. R. Polish[o,f], T. Prouve[n], C. Pryke[m], C. D. Reintsema[k], S. Richter[f], T. Romand[a], M. Salatino[h], A. Schillaci[a], B. Schmitt[f], R. Schwarz[m], C. D. Sheehy[m], B. Singari[m,t], A. Soliman[i,a], T. St Germaine[f], A. Steiger[a], B. Steinbach[a], R. Sudiwala[b], G. P. Teply[a], K. L. Thompson[h], C. Tucker[b], A. D. Turner[i], C. Vergès[v,f], A. G. Vieregg[j], A. Wandui[a], A. C. Weber[i], J. Willmert[m], C. L. Wong[f,o], W. L. K. Wu[d,c,h], H. Yang[h], C. Yu[j], L. Zeng[f], C. Zhang[h]

[a] Department of Physics, California Institute of Technology, Pasadena, CA 91125, USA
[b] School of Physics and Astronomy, Cardiff University, Cardiff, CF24 3AA, United Kingdom
[c] Kavli Institute for Particle Astrophysics and Cosmology, Stanford University, Stanford, CA 94305, USA
[d] SLAC National Accelerator Laboratory, Menlo Park, CA 94025, USA
[e] Department of Physics and Astronomy, University of British Columbia, Vancouver, British Columbia, V6T 1Z1, Canada
[f] Center for Astrophysics, Harvard & Smithsonian, Optical and Infrared Astronomy Division, Cambridge, MA 02138, USA
[g] Department of Physics, University of Cincinnati, Cincinnati, OH 45221, USA
[h] Department of Physics, Stanford University, Stanford, CA 94305, USA
[i] Jet Propulsion Laboratory, California Institute of Technology, Pasadena, CA 91109, USA
[j] Kavli Institute for Cosmological Physics, University of Chicago, Chicago, IL 60637, USA
[k] National Institute of Standards and Technology, Boulder, CO 80305, USA
[l] Argonne National Laboratory, High Energy Physics Division, Lemont, IL 60439, USA
[m] School of Physics and Astronomy, University of Minnesota, Minneapolis, MN 55455, USA
[n] Service des Basses Températures, Commissariat à l'Énergie Atomique, 38054 Grenoble, France
[o] Department of Physics, Harvard University, Cambridge, MA 02138, USA
[p] Department of Physics, University of Illinois at Urbana-Champaign, Urbana, IL 61801, USA
[q] Department of Astronomy, University of Illinois at Urbana-Champaign, Urbana, IL 61801, USA
[r] Centre for Theoretical Cosmology, DAMTP, University of Cambridge, Wilberforce Road, Cambridge CB3 0WA, UK
[s] Kavli Institute for Cosmology Cambridge, Madingley Road, Cambridge CB3 0HA, UK
[t] Minnesota Institute for Astrophysics, University of Minnesota, Minneapolis, MN 55455, USA
[u] Department of Physics, Boston University, Boston, MA 02215, USA
[v] Physics Division, Lawrence Berkeley National Laboratory, Berkeley, CA 94720, USA

***Abstract*—The BICEP/Keck collaboration searches for B-mode polarization in the Cosmic Microwave Background (CMB) as evidence of inflationary gravitational waves, with current best constraints placing $r_{0.05} < 0.035$. Building even deeper and larger maps requires scaling detector count at 150 GHz, where B-mode power is expected to peak at $\ell \sim 80$. The BICEP Array 150 GHz receiver (BA150) fields 7776 superconducting transition edge sensor (TES) detectors, over 15× the 512 deployed in the previous BICEP/Keck 150 GHz receiver, making it the densest time-division multiplexed readout receiver in the collaboration's history.**

We present the complete detector characterization of all 12 detector modules as deployed in BA150. We report thermal properties (T_c, G_c, $P_{\rm sat}$), end-to-end optical efficiencies of 20–48%, and fractional bandwidths of ∼28% across all modules. We additionally report the identification and mitigation of an out-of-band high-frequency photon leak spanning 180–265 GHz, and present preliminary investigations of elevated on-sky noise

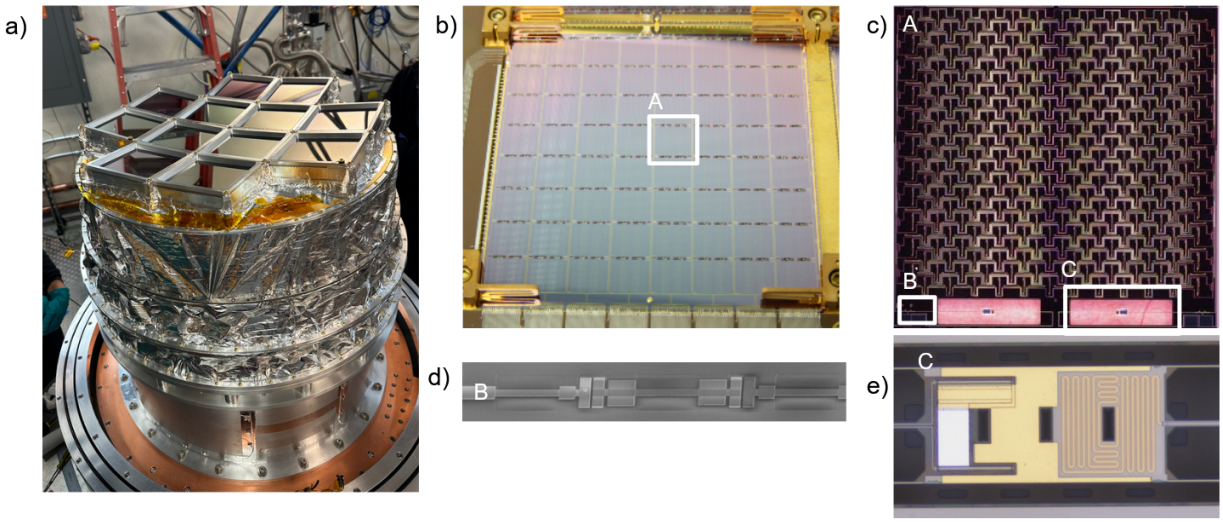

Fig. 1. (a) Photo of the BA150 receiver focal plane outfitted with 12 detector modules. (b) Photo of a Keck 150 detector module wafer. BA150 module wafers comprise of 18 x 18 pixels. (c) Each pixel contains a dual-polarization slotted antenna array coupled to two TES bolometers, with each bolometer receiving power from a single orthogonal linear polarization. (d) SEM image of the band-defining microstrip filter. (e) Image of the TES bolometer comprised of an island suspended on 6 silicon-nitride legs with one running a microstrip line to connect to the antenna, a gold resistive meander, a gold thermalizing block, and an Al TES and Ti TES connected in series.

attributed to aliased high-frequency detector noise.

***Index Terms*—BICEP Array, TES detectors, Inflation, CMB, BA150.**

I. Background

BICEP Array is the latest iteration of a legacy of experiments from the BICEP/Keck Collaboration working to measure evidence of cosmic inflation by deeply studying the polarization of the cosmic microwave background (CMB). Inflation theory dictates that the universe quickly expanded exponentially in size shortly after the Big Bang, and that such a process would produce primordial gravitational waves (PGWs). These PGWs would induce a divergence-free 'B-mode' polarization pattern in the CMB; measuring this polarization signal would therefore be direct evidence of inflation [1]. Inflationary models are therefore parametrized by the tensor-to-scalar ratio r, the amplitude of tensor perturbations (our PGWs) relative to scalar perturbations [2]. The BICEP/Keck collaboration has placed the strongest constraints on the tensor-to-scalar ratio to $r_{0.05} < 0.035$ at 95% confidence with $\sigma(r) = 0.009$ [3]. Achieving even deeper sensitivity requires increasing detector count on sky across a range of frequencies to also constrain polarized foregrounds.

BICEP Array is being actively fielded at the South Pole Station, and at completion will consist of 4 small aperture telescopes (SATs) observing across bands spanning 30 to 270 GHz. These receivers are designed to resolve $35 < \ell < 300$ features in an effective sky area spanning 600 $\deg^2$. The sensitive area of each receiver, referred to as the focal plane, contains 12 detector module slots. This design allows us to deploy receivers to the South Pole with a partial set of detector modules and observe while other modules are fabricated and characterized to be deployed in subsequent personnel deployment seasons. The focal plane of the BA30/40 receiver was completed at the South Pole in 2023, BA150 in 2024, and the BA220/270 receiver was deployed to the South Pole in 2024 with 3 modules, with ongoing efforts to fully populate its focal plane. The final receiver BA4 will target 90 and 150 GHz using a different coupling system than BICEP predecessors, instead using an orthomode transducer (OMT) coupled to a feedhorn.

II. Instrument

The BA150 receiver builds upon the highly vetted design of the BICEP3 receiver [4] [5]. The BA150 focal plane consists of 12 modules, each with 656 superconducting transition edge sensor (TES) detectors operated at 300 mK [6], 8 of which are optically dark detectors (TESes with no antennae connected) to aid in performance diagnostics. These detectors form pairs by being connected to a set of co-located, orthogonally polarized planar antenna arrays. Each detector is therefore sensitive to a single orthogonal linear polarization. Each detector pair forms a pixel which is tiled over a 6-inch silicon wafer in an 18x18 pixel grid. Each TES collects light from its respective antenna through band-defining filters, and BA150 is thus named as it is designed with a band center at 150 GHz, where we expect B-mode power to peak. If TES detectors are designed appropriately as expanded on in section A, they will be photon-noise dominated and therefore cannot be made more sensitive. As such, the only way to increase sensitivity using this technology is to scale up the detector count on sky. This has largely motivated the design of BICEP Array, vastly increasing our detector count over preceding receivers within the collaboration, as the last 150 GHz receiver deployed by the collaboration had 512 detectors in comparison to BA150's 7776.

Each TES detector is voltage biased into transition where it becomes a highly sensitive bolometer, changing resistance with temperature. The varying output current of the TES

is read out using superconducting quantum interference devices (SQUIDs) to perform low-noise amplification and time-domain multiplexing. Reading out all 7776 TES detectors in the BA150 focal plane with a multiplexing factor of 41 requires the use of 6 multi-channel electronics (MCE) readout systems, which were developed by the University of British Columbia [7]. Scaling up our detector density has necessitated re-design efforts to both the superconducting connections within a module [8] and to the nominal MCE design, condensing it so that two MCEs share a single frame so that all 6 MCEs could fit within the volume beneath the receiver while operating in the survey mount [9].

III. Detector Characterization

In order to validate our detectors, we perform several validation tests to measure critical parameters of our TES detectors. In this section we describe those measurement methods and discuss our resulting performance. All measured detector parameters of deployed modules are recorded in Table 1, where L is the designator name used for BA 150 modules. These 12 modules are selected from a total of 15 that were hybridized and tested. We note that modules L9 and L10 are missing from this table as those modules were found to perform below our design thresholds. One module, L11, had only its detector wafer replaced rather than being fully rejected, constituting the third module to fall below design thresholds. Note that thermal properties of the TES as described in subsection B could not be directly measured for several modules due to time constraints, so results marked with (*) indicate values that were estimated from dark detectors on modules that were tested under optically loaded conditions. T_c, the TES's critical temperature, could not be obtained for these modules. This is detailed further in subsection B.

A. TES Detector Design Principles and Goals

We first review some TES physics and how they inform our detector design and parameter goals.

The leading noise contributors in TESes are photon noise, phonon noise, and Johnson noise. The photon noise equivalent power (NEP) can be described as:

$$NEP_{\gamma}^2 = 2h\nu Q_t + \frac{2Q_t^2}{\nu\,\Delta\nu} \tag{1}$$

where ν is the band center, $\Delta\nu$ is the fractional bandwidth, and Q_t is the optical load on the detectors. Any measurement of photons has an intrinsic noise due to the quantized nature of light. Therefore when a detector is photon-noise dominated, we also refer to it as a quantum-limited detector. This represents the fundamental noise limit of a photon detector, and so we aim for it to be the dominant portion of our noise budget [10].

Phonon noise is determined by:

$$NEP_{\rm phonon}^2 = 4k_B T_c^2 G_c F \tag{2}$$

where T_c is the critical temperature of the TES, G_c is the thermal conductance of the TES island, and $F(T_c, T_0)$ accounts for the nonlinear thermal conductance between the TES island and the bath temperature and is conventionally assumed to be 0.5 [8].

TES detectors also exhibit thermal Johnson noise from both the TES itself and the shunt resistor used for voltage biasing:

$$NEP_{\rm Johnson}^2 = NEP_{\rm tes}^2 + NEP_{\rm sh}^2 \tag{3}$$

$$NEP_{\rm tes}^2 = 4k_B T_{tes} R_{\rm tes} I_{\rm tes}^2 \frac{1}{\mathcal{L}_i^2} \tag{4}$$

$$NEP_{\rm Johnson}^2 = 4k_B T_{\rm sh} R_{\rm sh} I_{\rm tes}^2 \frac{(\mathcal{L}_i - 1)^2}{\mathcal{L}_i^2} \tag{5}$$

where $\mathcal{L}_i$ is the TES loop gain, $R_{\rm tes}$ and $R_{\rm sh}$ are the TES and shunt resistances, T_{tes} and $T_{\rm sh}$ are their respective temperatures, and $I_{\rm tes}$ is the TES current. Johnson noise is suppressed by negative electrothermal feedback at high loop gain, making it typically a subdominant noise contributor.

In the transition region of the TES, we expect power on the island to be relatively constant over resistance if loop gain is high due to negative electrothermal feedback as optical and electrical power balance thermal power from the bath [10]. This flat power level is the saturation power of the TES ($P_{\rm sat}$). This is the amount of power that can be thermalized onto the TES, and if exceeded the detector will 'saturate', going into normal resistance where it will no longer act as a bolometer. $P_{\rm sat}$ is determined by:

$$P_{\rm sat} = \frac{G_c}{\beta + 1} \frac{T_c^{\beta+1} - T_0^{\beta+1}}{T_c^{\beta}} \tag{6}$$

where β is the thermal conductance exponent.

As stated before, TES detectors are quantum-limited when $\mathrm{NEP}_{\rm phonon}$ is subdominant to NEP_{γ}. Since $\mathrm{NEP}_{\rm phonon} \propto G_c$ (Eq. 2), selecting a lower G_c improves sensitivity, but also increases the bolometer's thermal time constant, and reduces $P_{\rm sat}$ (Eq. 6) which increases the risk of saturating on sky. We therefore estimate the expected optical load during sky observations and apply a safety factor to that optical load to produce a target P_{sat}. Using Eq. 6 we can then calculate a target G_c. And so given an expected on-sky loading of ~ 3.6 pW at 150GHz and a safety factor of 2.5, we target $P_{\rm sat} = 9.0$ pW. Assuming $T_c = 500$ mK, $\beta = 2$, and $T_0 = 270$ mK, this yields a target $G_c = 64$ pW/K. At this design point, we expect $\mathrm{NEP}_{\rm phonon} \approx 21.1\ \mathrm{aW}/\sqrt{\mathrm{Hz}}$, compared to $\mathrm{NEP}_{\gamma} \approx 33.4\ \mathrm{aW}/\sqrt{\mathrm{Hz}}$, confirming that the target G_c keeps the detector in the photon-noise-dominated regime.

B. Thermal Properties

We first discuss the measurement method for T_c, G_c, β, and $R_{n,\mathrm{Ti}}$.

We measure $P_{\rm sat}$ by taking load curves at various focal plane temperatures, and then fit for β, G_c, and T_c. Our test cryostat is able to reach a base temperature of 270 mK, and a heater on the UC stage is used to raise the focal plane temperature. Load curves consist of sweeping the bias of the TES and measuring the current produced, thus giving us an IV curve (Fig. 2a). This can then be converted into

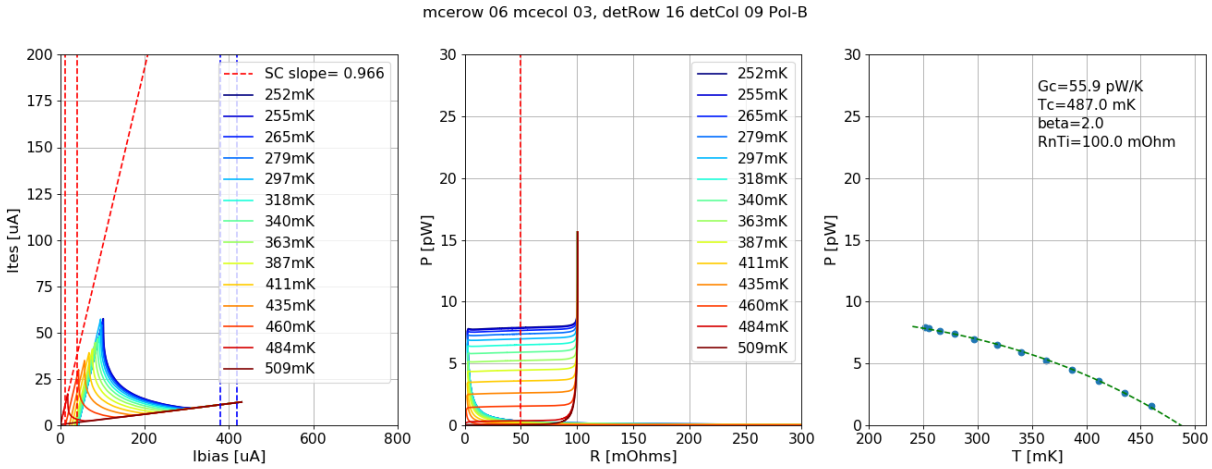

Fig. 2. Left: A series of IV curves taken on a single Ti TES in dark configuration over varying bath temperature. $I_{\rm bias}$ is the current applied across a 3mΩ shunt resistor to voltage bias the TES. Center: IV curves converted into PR curves; the vertical red line indicates where we take $P_{\rm sat}$ at a fixed R. Right: Fitting $P_{\rm sat}$ vs. T_0 using Eq. 6 to derive thermal properties of the TES.

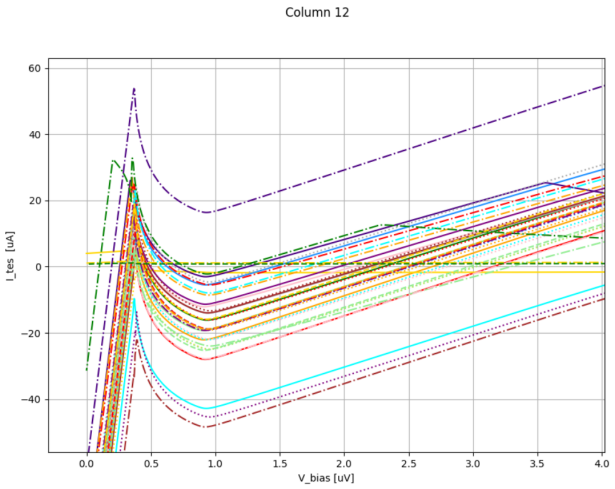

Fig. 3. Ti IV curves of several detectors on 1 column demonstrating uniform alignment and ease of biasability. We see that the transitions of all the TESes on this column are well aligned between 0.5-1μV, meaning that optimizing the bias across them becomes trivial.

a curve of power vs resistance, and $P_{\rm sat}$ is obtained in the flat section of the transition region of the curve shown in Fig. 2b. These measurements must be taken with the module in a dark configuration with all optical power eliminated by blanking optics off within the cryostat so that $P_{\rm sat} = P_{\rm electrical}$ and the power on the TES is only determined by the voltage bias we apply. We can then perform a multi-variable fit using Eq. 6 given measured P_{sat} at each T_b to derive G_c, T_c, and β as seen in Fig. 2c. $R_{n,\rm Ti}$ is derived from the IV curve where the detector is biased high enough to exhibit normal resistance [11] [12].

Unfortunately, time constraints due to our deployment schedule prevented us from testing every module in both light and dark configuration, and so for modules without dark testing G_c is estimated in Table 1 by measuring $P_{\rm sat}$ from dark detectors on each module, and assuming $T_c = 500$ mK and $\beta = 2.0$ which our modules have adhered well to.

Table 1 shows that we have some variation in G_c over modules, ranging from 50.0 to 140.0 pW/K. L1 and L2 are the earliest modules produced and have significantly higher G_cs, which decreased as we refined the fabrication process. Our bolometer geometries require TES island legs that are notably thinner and longer than those used by similar projects. Our bolometer legs are 535 μm long compared to ACTPol, which uses 35 μm [13]. We have found that we therefore seem to be more susceptible to potential roughening introduced by various fabrication steps. This has been seen historically throughout modules produced for the BICEP/Keck collaboration as moderate variances in G_c and therefore P_{sat} [12]. L3 is the only module fabricated with a modified recipe during our initial recipe refinements, which we suspect has led to its higher median $R_{n,\rm Ti}$. L12, though fabricated with the same recipe as the majority of modules, demonstrates a significantly lower G_c and $P_{\rm sat}$ than designed for. While these deviations are not ideal and this module saturates more frequently during sky observations, it is also correspondingly our most sensitive module. After considering the amount of data lost due to saturation against the higher sensitivity, we have opted to continue observing with it. The variances seen for modules produced for BA150 are otherwise within expectation from what we have seen with previous detector fabrication runs and are largely on target for the sensitivities required.

C. Biasability

We are also interested in measuring $R_{n,\rm Ti}$ for two critical reasons. The first reason is that TES Johnson noise increases with $R_{n,\rm Ti}$, though it is usually a small contributor. The second, and arguably more important reason is that each voltage bias line is shared by 41 detectors, and variations in $R_{n,\rm Ti}$ will shift the range of electrical biases that a TES's transition range occupies. Therefore if there is a large variation in $R_{n,\rm Ti}$, it becomes difficult to optimally bias all detectors in one bias line. We have observed R_n of our TESes to be very uniform and we have experienced little issue in biasability as demonstrated in Fig. 3.

TABLE I
BA150 DETECTOR PARAMETERS

Parameter	L1	L2	L3	L4	L5	L6	L7	L8	L11	L12	L13	L14
Wafer yield	98.5%	97.2%	94.0%	95.1%	97.5%	98.3%	94.4%	93.8 %	97.6 %	98.8 %	95.7 %	96.7 %
Readout yield	80.8%	92.7%	77.7%	97.9%	74.4%	94.4%	86.0%	98.2%	98.3%	98.0%	86.7%	98.2%
G_c (pW/K)	105.19 ± 7.52	139.87 ± 13.50	53.19 ± 5.90	51.25 ± 3.84	91.3 (*)	49.99 ± 5.23	59.57 (*)	52.21 (*)	54.12 (*)	81.74 (*)	59.11 (*)	76.60 (*)
T_c (mK)	511.27 ± 4.28	528.73 ± 8.53	540.78 ± 7.51	483.64 ± 6.54	–	489.43 ± 4.60	–	–	–	–	–	–
$P_{\rm sat}$ (270 mK)	15.29 ± 1.14	21.36 ± 2.09	8.38 ± 0.85	6.82 ± 0.56	9.0 (*)	6.78 ± 0.69	8.6 (*)	7.33 (*)	7.60 (*)	4.44 (*)	7.72 (*)	10.01 (*)
$R_{n,\rm Ti}$ (mΩ)	58.92 ± 0.31	68.51 ± 0.90	132.25 ± 2.62	87.90 ± 2.08	74.09 ± 0.71	71.32 ± 0.58	100.93 ± 2.01	83.53 ± 4.65	84.08 ± 2.53	78.99 ± 1.86	85.97 ± 3.76	72.60 ± 2.97
End-to-End OE (%)	20.64 ± 0.10	39.06 ± 0.49	19.15 ± 0.19	32.77 ± 0.11	33.70 ± 0.48	24.82 ± 0.19	39.54 ± 0.29	40.12 ± 0.39	42.09 ± 0.27	47.96 ± 0.41	40.14 ± 0.42	35.00 ± 0.31
Bandwidth (%)	28.71 ± 0.85	28.79 ± 0.50	28.35 ± 1.00	28.28 ± 0.58	29.07 ± 0.50	27.48 ± 1.04	28.30 ± 0.66	28.31 ± 1.06	27.60 ± 1.76	28.90 ± 1.98	27.28 ± 2.60	27.87 ± 1.27
Band Center (GHz)	146.7 ± 1.25	148.4 ± 0.72	147.0 ± 1.48	148.0 ± 0.54	146.9 ± 0.57	149.9 ± 1.39	146.8 ± 0.96	149.0 ± 1.03	147.6 ± 0.99	149.2 ± 1.05	148.0 ± 1.85	150.1 ± 1.88

All parameters quoted as median and standard error over detectors measured across the 12 deployed BA150 modules, selected from 15 hybridized and tested. Modules L9 and L10 were excluded for performance below design thresholds.
* Value estimated from optically dark detectors (TES islands with no antenna) on modules tested under optical loading. T_c could not be obtained for these modules.

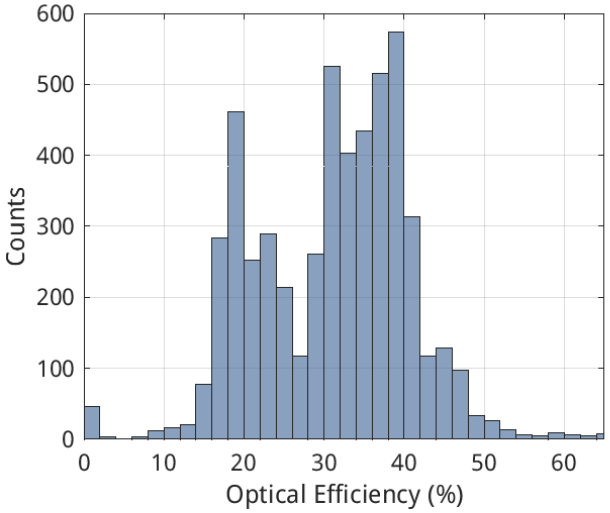

Fig. 4. End-to-end optical efficiency over all detectors in BA150.

D. Optical Performance

We measure end-to-end optical efficiency by placing two aperture-filling black body sources at 300 K and 77 K using liquid nitrogen. By measuring both the change in $P_{\rm sat}$ under both optical loads and our fractional bandwidth, we can then compute optical efficiency. We write the expected change in power while observing different temperature black bodies as:

$$\Delta P = \int_0^\infty A\Omega\,\eta(\nu)\,\frac{\nu^2 k_B \Delta T}{c^2}\,d\nu = k_B \Delta T \int_0^\infty \eta(\nu)\,d\nu \tag{7}$$

where ΔP is the total power change seen on the TES given different optical load temperatures, $A\Omega$ is the antenna throughput, equal to λ^2 for a single-mode antenna, and ΔT is the difference in temperature of the two black bodies. We define the full-band optical efficiency η in Eq. 7 as:

$$\eta = \frac{dP/dT}{k_B\,\Delta\nu} \tag{8}$$

Optical efficiency only depends on the power delivered by components of the optical path, namely the optical filters, optics, antennae, and band defining filters, but not on the TES material. We have two TESes in series of differing materials with different T_cs. We are therefore able to optically test our detectors in the lab observing ~ 300 K without using a neutral density filter by having an Al TES with a $T_c \approx 1$ K in series with our science Ti TES with $T_c = 500$ mK, as the titanium TES would otherwise be saturated as it is designed to observe the ~ 20 K sky at the South Pole. This allows us to directly measure our full end-to-end optical efficiency and antennae bandpasses without adding components to our optical path.

Optical efficiencies reported in Table 1 are dark-corrected, meaning we have subtracted the non-negligible $\frac{dP}{dT}$ measured on optically dark detectors on each module, which is uniformly on the order of $\approx 4 \times 10^{-3}$ pW/K across all modules. This pickup has generally been attributed to features on the TES island directly coupling to light. This topic will be expanded upon in section 4.

Optical efficiency has varied from module to module, generally ranging from 20–48%. Some outliers include L3 which used a different TES island from all other modules, and L6 which has presented with a notch within its bandpass at $\sim$ 161 GHz which would impact optical efficiency. L6 has a longer leg length of 800 μm instead of 535 μm that other modules use, and this is being investigated for potentially causing reflections of incident power. Aside from these outliers, optical efficiency has met or exceeded our targets.

IV. CHARACTERIZATION OF OUT-OF-BAND PICKUP

While taking optical efficiency data, the optical response on optically dark detectors was found to be significantly greater than expected. Due to suspicions of out-of-band photon pickup which has shown up on TESes before, we devised tests to characterize the potential power and spectral location of a high-band leak.

Given Eq. 1, one can observe that photon noise increases with frequency, and so we are especially concerned about the

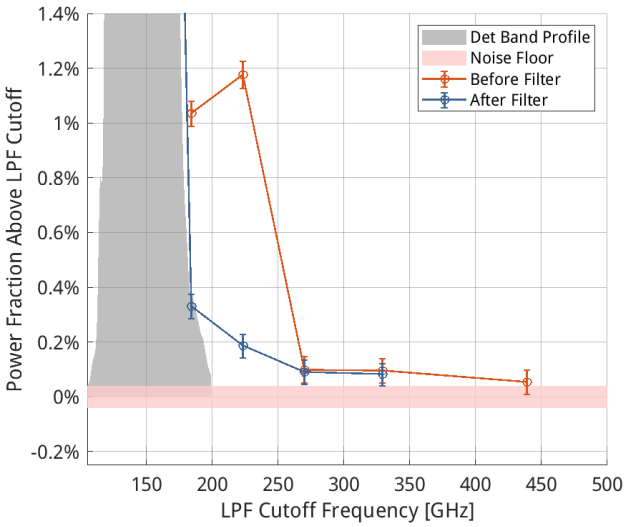

Fig. 5. Measured optical signal before and after installation of the LPE (low pass edge) filter in 2024 to cut the high-frequency leak. The measured average co-added antenna band is included in grey to demonstrate our bandwidth, but is not to scale. The 1σ noise floor without any incident power is shown in red.

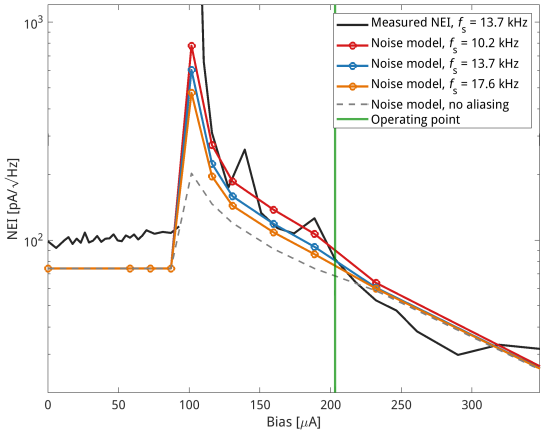

Fig. 6. Measured NEI as a function of current bias for a single detector, compared to noise model predictions. Lines show the baseline model with no aliasing and models with aliased noise contributions calculated from 50 MHz superfast noise measurements at sampling rates of 10.2, 13.7, and 17.6 kHz. Including aliased noise brings model predictions into agreement with the measured data, indicating that elevated on-sky noise is well-explained by high-frequency detector noise aliasing into the science band.

pickup of photons above our design band. The upper band edge for BA150 detectors is around 180 GHz, and we therefore focus our studies between 180 GHz and 500 GHz where we have a low-pass nylon filter cutoff.

A set of thick grille filters (TGFs) were prepared to bring to the South Pole in 2023. These metal filters are metal plates machined out with a dense pattern of holes, and the diameter of these holes sets the high-pass cut-off frequency of each filter. These filters are then placed over the output aperture of an optically chopped black body hot source that is positioned over the receiver window. We take a dataset per filter which spans from 180–439 GHz. In addition to all filtered data, two control datasets are taken, one with a solid metal plate placed where the filters go, and one with no filters at all. The former is to get a 'light leak' dataset, which gives us the characteristic noise floor by blocking the chopped source. The latter, or 'no filter' dataset measures our full spectrum response.

Each 10 min dataset is then phase-synchronously demodulated. The data is split into 10 sections of 1 min each to overcome the source chopper's wandering chop frequency of $\sim$ 0.2 Hz over the whole 10 min timestream. In order to collect amplitude information without noise bias, we shift the detector timestreams to match the phase of the chop signal. The shift is identified by taking the cross correlation of all detector signals with the chopper signal, finding the time shift that gives maximum correlation for each detector, and taking the mode of this shift over all detectors. This assumes the delay seen on each detector is largely generated by the delay between the physical chopper's blade and its output chop reference, and that the delay between different detectors is negligible. This was checked by comparing the cross correlation of detectors after this first phase shift and finding little drift between detectors. This demodulated amplitude is then collected per 1 min section of each dataset over all detectors. This is all done in order to maximize our sensitivity to this low pickup.

We found a large, broadband signal above 180 GHz and ending approximately at 265 GHz that accounted for $\sim 1\%$ of the total power deposited onto the TES. With the introduction of a 6.2 cm^{-1} low-pass edge (LPE) filter provided by Cardiff and installed during the 2024 austral summer season, we were able to repeat TGF measurements as shown in Figure 5. The LPE filter reduced total out-of-band power by $\approx 70\%$. Above 265 GHz, before- and after-filter measurements are consistent, indicating the leak is confined to the 180–265 GHz range. The origin of the leak is suspected to arise from direct absorption of incident power onto the TES island itself rather than through the antenna, though this has not yet been confirmed.

V. Noise Characterization

With all detector parameters measured we can then proceed to produce predictions of expected noise performance in Noise Equivalent Current (NEI) and Noise Equivalent Temperature (NET), and then compare our models to noise measurements on sky to see if our performance meets our expectations. In doing so we have seen evidence of elevated noise in our detectors that we are actively investigating. High-bandwidth noise measurements on single detectors allow us to characterize our noise far above our normal sampling rate to check for noise that will alias down into our band during regular operations. Noise stare measurements at various TES biases are compared to model predictions while adding measured aliased noise values from superfast noise measurements, and preliminary results indicate that the main contributor to our elevated noise is indeed coming from detector noise at high frequencies getting aliased down into our band during sampling. Preliminary analyses demonstrate that the loop gain of our detectors is significantly higher than expected, causing our detector bandwidths to increase past our design limits and increasing aliased noise at our sampling frequency. Higher loop gain was observed following modifications to the TES

fabrication process made to address low loop gain in earlier BA30/40 modules [11], but these corrections appear to have overshot the target. These results are shown in Fig. 6 and will feature in future proceedings.

VI. Conclusion

We have presented measurements of the key detector parameters for the BA150 transition-edge sensor (TES) arrays used in the BICEP Array experiment. Across all tested modules, the thermal conductance G_c, critical temperature T_c, normal resistance $R_{n,\mathrm{Ti}}$, band centers, bandwidths, and end-to-end optical efficiencies are broadly consistent with design expectations, with some module-to-module variation attributable to fabrication process refinements. Noise characterization reveals elevated on-sky noise consistent with high-frequency detector noise aliasing into the science band, attributed to higher-than-designed loop gain arising from TES fabrication process adjustments. These results establish the current performance baseline of BA150, and ongoing efforts to reduce operating detector loop gain are expected to bring noise performance closer to design targets in future observing seasons.

In addition to standard detector characterization, we conducted a targeted investigation of a high-frequency leak identified during testing. We measured its amplitude and spectral location, finding a sub-percent, high-frequency diffuse band leak. These measurements guided improvements to the filter stack, reducing potential systematic contamination in future deployments.

The accurate characterization of detector properties and identification of out-of-band features are essential for achieving BICEP Array's scientific objectives. With validated detector performance, BA150 will contribute to multi-frequency measurements of the cosmic microwave background B-mode polarization, acquiring deeper signal maps to support the collaboration's foreground separation and delensing efforts. Combined with the BICEP/Keck analysis framework demonstrated in previous publications [3], BA150 is positioned to contribute strongly to future constraints on r as performance refinement efforts progress.

Acknowledgments

The BICEP/Keck experiments have been funded through U.S. National Science Foundation grants most recently including 2220444-2220448, 2216223, 1836010, and 1726917. The development of antenna-coupled detector technology was supported by the Jet Propulsion Laboratory Research and Technology Development fund. The research was carried out at the Jet Propulsion Laboratory, California Institute of Technology, under a contract with the National Aeronautics and Space Administration (80NM0018D0004). Focal plane development and testing were supported by the Gordon and Betty Moore Foundation at the California Institute of Technology. Readout electronics were supported by the Canada Foundation for Innovation grant to the University of British Columbia. The computations in this paper were run on the Cannon cluster supported by the FAS Science Division Research Computing Group at Harvard University. The analysis effort at Stanford University and the SLAC National Accelerator Laboratory was partially supported by the Department of Energy. We thank the staff of the U.S. Antarctic Program and in particular the South Pole Station without whose help this research would not have been possible. We also thank our winter-over operators: Manwei Chan, Karsten Look, Calvin Tsai, Paula Crock, Ta Lee Shue, Grantland Hall, Hans Boenish, Robert Schwarz, Sam Harrison, Anthony DeCicco, Thomas Leps, Brandon Amat, Nathan Precup, Steffen Richter, Thibault Romand, Danielle Simmons, Markus Ayasse, and Steven Jungst.

References

[1] U. Seljak and M. Zaldarriaga, "Signature of Gravity Waves in the Polarization of the Microwave Background," *Phys. Rev. Lett.*, vol. 78, pp. 2054–2057, 1997.

[2] M. Kamionkowski, A. Kosowsky, and A. Stebbins, "A Probe of Primordial Gravity Waves and Magnetic Fields with CMB Polarization," *Phys. Rev. Lett.*, vol. 78, pp. 2058–2061, 1997.

[3] BICEP/Keck Collaboration (P. A. R. Ade et al.), "BICEP/Keck Constraints on Primordial Gravitational Waves using Planck, WMAP, and BICEP/Keck Array Data," *Phys. Rev. Lett.*, vol. 127, 151301, 2021.

[4] BICEP/Keck Collaboration, P. A. R. Ade *et al.*, "BICEP/Keck XV: The BICEP3 Cosmic Microwave Background Polarimeter and the First Three-year Data Set," *Astrophys. J.*, vol. 927, no. 1, p. 77, 2022.

[5] Howard Hui et al., "BICEP Array: a multi-frequency degree-scale CMB polarimeter," Proc. SPIE 10708, 1070807, 2018. (arXiv:1808.00568, DOI:10.48550/arXiv.1808.00568)

[6] BICEP2, Keck Array, and SPIDER Collaborations, P. A. R. Ade *et al.*, "Antenna-Coupled TES Bolometers Used in BICEP2, Keck Array, and SPIDER," *Astrophys. J.*, vol. 812, no. 2, p. 176, 2015.

[7] E. S. Battistelli et al., "Functional description of read-out electronics for time-domain multiplexed bolometers for millimeter and submillimeter astronomy," *J. Low Temp. Phys.*, vol. 151, no. 3–4, pp. 908–914, May 2008.

[8] A. Schillaci et al., "BICEP Array: 150 GHz detector module development," Nov. 29, 2021, arXiv: arXiv:2111.14785.

[9] S. Fatigoni, "Constraining the inflationary universe from the South Pole," 2023, doi: 10.14288/1.0427409.

[10] K. D. Irwin and G. C. Hilton, "Transition-Edge Sensors," *Cryogenic Particle Detection 99*, pp. 63–149, 2005.

[11] C. Zhang, "The Development and Performance of the First BICEP Array Receiver at 30 and 40 GHz for Measuring the Polarized Synchrotron Foreground," Ph.D. dissertation, California Institute of Technology, 2023, doi: 10.7907/bfsb-6438.

[12] H. Hui, "Measuring the Polarization of the Cosmic Microwave Background with BICEP3," Ph.D. dissertation, California Institute of Technology, 2018, doi: 10.7907/G8ET-FD62.

[13] R. J. Thornton, P. A. R. Ade, S. Aiola *et al.*, "The Atacama Cosmology Telescope: The Polarization-Sensitive ACTPol Instrument," *Astrophys. J. Suppl. Ser.*, vol. 227, no. 2, p. 21, 2016.